Biosensors and Bioelectronics 295 (2026) 118260

Contents lists available at ScienceDirect

Biosensors and Bioelectronics

journal homepage: www.elsevier.com/locate/bios

Bio-hybrid Photovoltaic devices operated on living photosynthetic bacteria

Rossella Labarile [a,1], Anna De Salvo [b,1], Federico Rondelli [b,c], Maria Michela Giangregorio [d], Michele Di Lauro [b,*], Massimo Trotta [a,**], Gianluca Maria Farinola [e,1], Fabio Biscarini [b,f,1]

[a] Consiglio Nazionale delle Ricerche, Istituto per i Processi Chimico Fisici, via E. Orabona 4, Bari, 70125, Italy
[b] Fondazione Istituto Italiano di Tecnologia, Center for Translational Neurophysiology of Speech and Communication, Fondazione, via Fossato di Mortara 17/19, Ferrara, 44121, Italy
[c] Università di Ferrara, Sezione di Fisiologia Dipartimento di Neuroscienze e Riabilitazione, via Fossato di Mortara 17/19, Ferrara, 44121, Italy
[d] Consiglio Nazionale delle Ricerche, Istituto di Nanotecnologia, via E. Orabona 4, Bari, 70125, Italy
[e] Università degli Studi di Bari A. Moro, Dipartimento di Chimica, via E. Orabona 4, Bari, 70125, Italy
[f] Università di Modena e Reggio Emilia, Dipartimento di Scienze della Vita, via Campi 103, Modena, 41125, Italy

ARTICLE INFO

Keywords:
Biophotovoltaics
Biohybrid devices
Photosynthetic bacteria
Photovoltage generation

ABSTRACT

The use of the abundant and easily available solar energy is central towards a carbon-free society and represents the most sustainable strategy for the increasing energy demand. *Rhodobacter (R.) sphaeroides* is a versatile photosynthetic purple non sulfur bacteria able to harvest sunlight, particularly in the Near InfraRed (NIR) region, and to efficiently transform it into photochemical energy. In this work, whole wild-type, metabolically-active photosynthetic bacterial cells of *R. sphaeroides*, and their carotenoid-less mutant strain, were integrated in a two-electrode architecture, to output a positive photovoltage upon illumination. The photovoltage amplitude of the mutant strain is almost three times higher than that obtained with wild-type cells. Photosynthetic bacteria were also integrated in a light-electrolyte-gated organic transistor to produce a photomodulated electronic current, as well as in a biophotonic power cell working on direct sunlight. This proves that bio-organic hybrid optoelectronic devices may enable environmentally safe and cost-effective energy production.

1. Introduction

In the context of global environmental concerns (Guang-Wen et al., 2022; Peisker, 2023; Yolcan, 2023; Zhang et al., 2022), the current dependence on fossil fuels (Mayer, 2022) quests for the production of energy from renewable sources (Jaiswal et al., 2022; Wang and Azam, 2024). Starting from the consideration that the daily world energy need is 10,000 times lower than the approximate number of terawattshour of solar energy that shines on the Earth each day, harvesting energy directly from sunlight appears to be a most promising approach (Rhodes, 2010) towards a carbon-neutral society and represents a most desirable sustainable path towards the increasing energy demand (Holechek et al., 2022; Qazi et al., 2019; Rather et al., 2022). In addition, solar energy has the potential to be produced in almost any territory around the globe. Thus, there is a need to develop strategies for the efficient exploitation of the abundant and easily available energy of the sun (Chen et al., 2023; Pourasl et al., 2023) enabling solar powered technologies (Chinipardaz et al., 2024).

The study of photosynthesis and its mechanisms provides insights about fundamental mechanisms of photochemical energy conversion (Sekar et al., 2014). In turn, photosynthesis inspired researchers to develop artificial photosynthetic systems (Brown and King, 2020; El-Khouly et al., 2017; Kathpalia and Verma, 2021; Utschig, 2020) that mimic, in parts, the function of the intricate molecular machinery that is the core of this paramount metabolic process (Ravi and Tan, 2015). Only photosynthetic organisms, namely plants, algae and some bacteria, can directly exploit sunlight to synthesize energy-rich compounds from abundant and thermodynamically stable feedstocks like water, sulphidric acid, and CO_2. They were finely tuned over billions of years of evolution to manage photon capture and conversion processes. A significant, widely investigated, example of photosynthetic anoxygenic microorganisms is the purple non-sulfur bacterium *Rhodobacter* (*R.*) *sphaeroides*, which absorbs light by means of its antenna system (Hu et al., 2002; Scheuring et al., 2014; Timpmann et al., 2014), yielding

* Corresponding author.
** Corresponding author.
E-mail addresses: massimo.trotta@cnr.it (M. Di Lauro), michele.dilauro@iit.it (M. Trotta).
[1] Rossella Labarile and Anna De Salvo contributed equally to this work. Gianluca Maria Farinola and Fabio Biscarini contributed equally to this work.

https://doi.org/10.1016/j.bios.2025.118260
Received 28 May 2025; Received in revised form 15 October 2025; Accepted 21 November 2025
Available online 21 November 2025

electron transfer (and correlated proton transfer) across the inner membrane, by the action of a key photoenzyme termed reaction center (RC).

Mimicking photosynthesis (Liu et al., 2024) by functionally integrating natural photosynthetic machinery in technological solutions is a rational approach to the problem of transforming light into electrical energy, but it requires to interface photosynthetic apparata with organic and/or inorganic materials for charge transport and storage (Berry et al., 2004; Cooley et al., 2009; Kornienko et al., 2018; Lawrence et al., 2023; Lukashev et al., 2007; Musazade et al., 2018; Walker, 1998). Most of these biohybrid device architectures are based on proteins immobilized, via adhesion layers or membranes, on electrode surfaces, either smooth or structured, working in a liquid electrolyte (Csiki et al., 2018; Das et al., 2004; Trammell et al., 2004). Physisorption of RCs on multi-layer graphene electrodes or on poly-aniline-covered porous silicon pillars provides remarkable photocurrent densities ranging from nA/cm^2 to μA/cm^2 upon light exposure, in the presence of bio-functional redox mediators such as ubiquinone (Das et al., 2004; Operamolla et al., 2015; Trammell et al., 2004). Other strategies to increase photocurrent involve multi-layer RC deposition and modulation of the intensity of the excitation light source (Hajdu et al., 2022).

Besides photocurrent, bio-hybrid architectures can be aimed at photovoltage generation. The capability of a bio-hybrid electrode to sustain a potential difference upon light exposure could be also exploited in device architectures operated in electrolytic environments as a novel approach towards light harvesting and conversion. The magnitude of photogenerated voltage scales with the amount of RCs added to a supporting transparent electrode, previously coated with oxidized cytochrome *c* (*cyt c*) (Di Lauro et al., 2020a). Noticeably, the use of pre-oxidized *cyt c* as grafting agent for RCs prevents electron transfer to the electrode and sustains the photovoltage in time, following a paradigm which is opposite to the use of redox mediators in photocurrent-based strategies, viz. Preventing the cascade of redox reactions associated to the primary electronic excitation. Upon NIR illumination, it was possible to achieve a voltage density as high as 296 ± 20 mV/cm^2 on ITO electrodes functionalized by 16 nmol/cm^2 *cyt c* and 14.6 nmol/cm^2 RC (Di Lauro et al., 2020a). Such photogenerated voltage was then exploited to modulate the output current of electrolyte-gated organic transistors (EGOTs) (Di Lauro et al., 2019).

EGOTs (Rivnay et al., 2018) are low-power three-terminal devices, achieved by contacting an active channel, constituted by an organic thin-film, with two electrodes, termed Source and Drain. The channel, which can be made of either an Organic Semi-Conductor - OSC - or an organic mixed ionic-electronic conductor - OMIEC, is directly exposed to an electrolyte, whose potential is set by a third electrode, termed Gate.

A small variation of the (electro)chemical potential of the electrolyte results in an amplified variation of the channel conductivity, which is a convenient principle for converting ionic signals from a biological environment into electronic current signals (Giordani et al., 2020; Marquez et al., 2020; van de Burgt et al., 2023). Several EGOT applications were demonstrated, encompassing bio-/chemo-sensing, electrophysiological signal transduction, transport across tight-cell junctions and monolayers, up to the most recent neuromorphic organic electronics, where the dynamics of ion fluxes induced by pulsed voltages causes “plasticity” and memory effects in the EGOT response (Di Lauro et al., 2020b, 2022; Harikesh et al., 2022; Rondelli et al., 2023). Most of these applications require tailored functionalization of the gate electrode with a single macro- or bio-molecular system, specific for the envisioned task. As an example, the light-modulated EGOT requires the above described gate functionalization with RCs.

The use of metabolically active photosynthetic microorganisms rather than RCs, would overcome the limitations of enzyme extraction, isolation, and purification protocols. Moreover, it would enable a sustainable technology for energy production, that is intrinsically ubiquitarian and suitable for distributed application in settings also characterized by low technology level. In this work, we investigate light-sensitive bio-hybrid electrodes fabricated with whole bacteria of the wild-type strain of *R. sphaeroides* adsorbed onto a conductive ITO/glass electrode. Photovoltage generation and storage are investigated upon different lighting conditions. We compare the output from wild-type *R. sphaeroides* with that of its well-known R26 mutant strain lacking carotenoids (Clayton, 1960; Clayton and Smith, 1960), to highlight the role of photoprotectors in voltage generation and to assess long-term stability and feature reproducibility of the proposed architecture.

The performances of the two bacterial strains are compared at different pH, to assess the plasticity of the bio-hybrid device and the ability to train it with suitable light pulses. The photoactive electrodes are finally integrated in a light-driven EGOT (LEGOT) and in a power cell driven by direct sunlight illumination, demonstrating the capability to sustain a functionally exploitable bias. Bio-hybrid optoelectronic devices based on whole metabolically active photobacteria represent a novel strategy for environmentally safe and cost-effective energy production and storage.

2. Experimental section

2.1. Microbial growth

Strain 2.4.1 and R26 of *R. sphaeroides* were grown in bacterial medium (Buccolieri et al., 2006; Giotta et al., 2006; Labarile et al., 2025) in anoxygenic condition. After incubation at room temperature for 3 h in the dark for the consumption of residual oxygen, the liquid cultures were exposed to steady illumination by quartz halogen lamp 80 W at 28 °C. Cell densities, expressed in CFU mL^{-1}, were extracted from the absorbance value at 660 nm, using a Lange turbidimeter (Buccolieri et al., 2006). Steady-state optical spectra of bacterial strains were recorded by a Cary 5000 (Agilent) UV–visible–near infrared (NIR) spectrophotometer, harvested, washed, and resuspended in 5 mM phosphate 1 mM EDTA at pH 8.

2.2. Atomic force microscopy analysis

Film morphology and aggregation state were imaged using atomic force microscopy (AFM) in contact mode (C-AFM) using an Autoprobe CP-Thermomicroscope. A sharp conical tip with a radius of curvature <10 nm mounted on a p-type doped Si cantilever was used.

2.3. Electrochemical Impedance Spectroscopy

Electrochemical Impedance Spectroscopy (EIS) was used to characterize the electrochemical properties of ITO electrodes colonized with bacterial cells. A bare ITO electrode served as the control. All measurements were conducted using a potentiostat/galvanostat equipped with a Frequency Response Analyzer (FRA) in two-electrode configuration. EIS data were acquired by applying a sinusoidal AC voltage signal with an amplitude of 10 mV over a frequency range from 500 kHz down to 10 mHz. Measurements were performed at the open circuit potential of the system, which was allowed to stabilize for at least 5 min before data acquisition.

2.4. Photovoltage measurements

Chronopotentiometry (V *vs* t) curves upon illumination were acquired using channel 1 of a Keysight B2912A Source-Measure Unit in current control (I = 0 A) with a two-electrode configuration, connecting the bio-hybrid light-sensitive electrode and a Pt counter electrode (0.25 cm^2) to the high force and low force terminals of a Keysight N1294A-001 adapter, respectively. A 1 M phosphate-buffered saline solution (pH = 7.4) has been used as electrolyte, while NIR excitation has been provided using an MTE1081C LED (Marktech Optoelectronics). Signals have been acquired upon fast (30 s light/60 s dark, fNIR) and slow (100 s light/200 s dark, sNIR) lighting cycles, measuring the voltage variation (ΔV). The

peak-to-peak voltage variation was divided by the concentration of bacteria, expressed in terms of colony-forming units per mL (CFU mL^{-1}), obtaining the parameter Ξ. The average illumination and discharge profiles result from four consecutive cycles over three replicates for both lighting conditions. Time-constants of potential build-up profiles are obtained via exponential fit of the photovoltage vs time experimental data. Long-term operation and photo-conversion efficiency were evaluated by extracting the profile of the generated photovoltage. The performances of the two bacterial strains were also compared at different pH. Transfer curve was acquired with ITO gate electrode applying $V_{DS} = -0.7$ V. The V_{GS} was linearly scanned between −0.8 V and 0.8 V. For LEGOT characterization, transfer curves have been acquired upon the application of a drain-to-source bias, photo-current was recorded under two gate voltages using the lighting protocol of 30 s dark/60 s light.

3. Results and discussion

3.1. Photo-voltage measurement with light-sensitive bio-hybrid electrode

Light sensitive bio-hybrid electrodes can be obtained by drop-casting a known volume (50 μL) of bacterial suspension with known optical density onto ITO-coated glass slides. This straightforward method causes bacteria to adhere via non-covalent interactions, mainly consisting of coulombic attraction between the overall negatively charged bacterial surfaces (e.g. lipopolysaccharides) and amphoteric domains on the substrate (Lu et al., 2011) or van der Waals interactions, which play secondary roles depending on surface energy and roughness (Carniello et al., 2018; Li et al., 2021; Oh et al., 2018). ITO coverage can be monitored via Electrochemical Impedance Spectroscopy (see Experimental Section), as routinely done in the development of bio-functionalized electrodes (e.g. those used for the development of biosensors) (Ahmadi et al., 2021; Genitoni et al., 2025; Khoshfetrat, 2025; Khoshfetrat et al., 2024, 2025; Mousavi et al., 2017; Wang et al., 2024). Fig. S1 shows the typical comparison between EIS Bode plots of bare and coated ITO electrodes, emphasizing how coverage results in a significant shift of the characteristic relaxation frequency without the appearance of any novel charge transfer process, consistently with the deposition of a layer of faradically inert material. Fig. 1a depicts a schematic of the electrode fabrication and characterization workflow. Photovoltage at these electrodes, against a Pt counter electrode, can be acquired using the measurement setup described in the Methods section and shown in Fig. 1b. Prior to drop-casting, the photophysical properties of the wild-type 2.4.1 cells grown under anaerobic conditions were investigated by UV–Visible–NIR absorption spectroscopy (Fig. S2). Their spectrum shows the three carotenoid-related absorption peaks (in the region between 440 and 520 nm) and the three bacteriochlorophylls absorption peaks, characteristic of the LH2 and RC-LH1 complexes, at 590 nm, 800 nm, and 850 nm.

Atomic Force Microscopy (AFM) was employed to assess the surface morphology after bacterial deposition. The bare ITO surface exhibits a low root mean square (RMS) roughness of 3 nm (±1 nm), confirming its suitability as a pristine, flat baseline. Following bacterial deposition, a dramatic increase in roughness was observed for both the wild-type and R26 strains, indicating successful cell adhesion and coverage. The wild-type resulted in a surface roughness as high as 56 nm (±4 nm) while the R26 strain showed a roughness of 43 nm (±2 nm), suggesting that the mutant yields a more uniform and less topographically varied layer. Representative AFM images are now reported in Fig. S3.

In the typical photovoltage generation experiment, a potential difference of around 50 mV can be recorded between the bio-hybrid electrode and the Pt counter one in the dark. Upon NIR illumination of wild-type bacteria (here starting at t ≈ 3min) it is possible to generate a photovoltage as high as ~120 mV, which settles at around 80 mV after 10 min and can be sustained it for more than 40 min (Fig. 1c). Control experiments, on bare ITO electrodes, do not show photovoltage generation (Fig. S4 in the Supporting Information).

To the best of our knowledge, this is the first report of photovoltage generation from intact bacteria. Table S1, in the Supporting Information, reports a comparative table between these results and results from related, although different, architectures, such as those based on

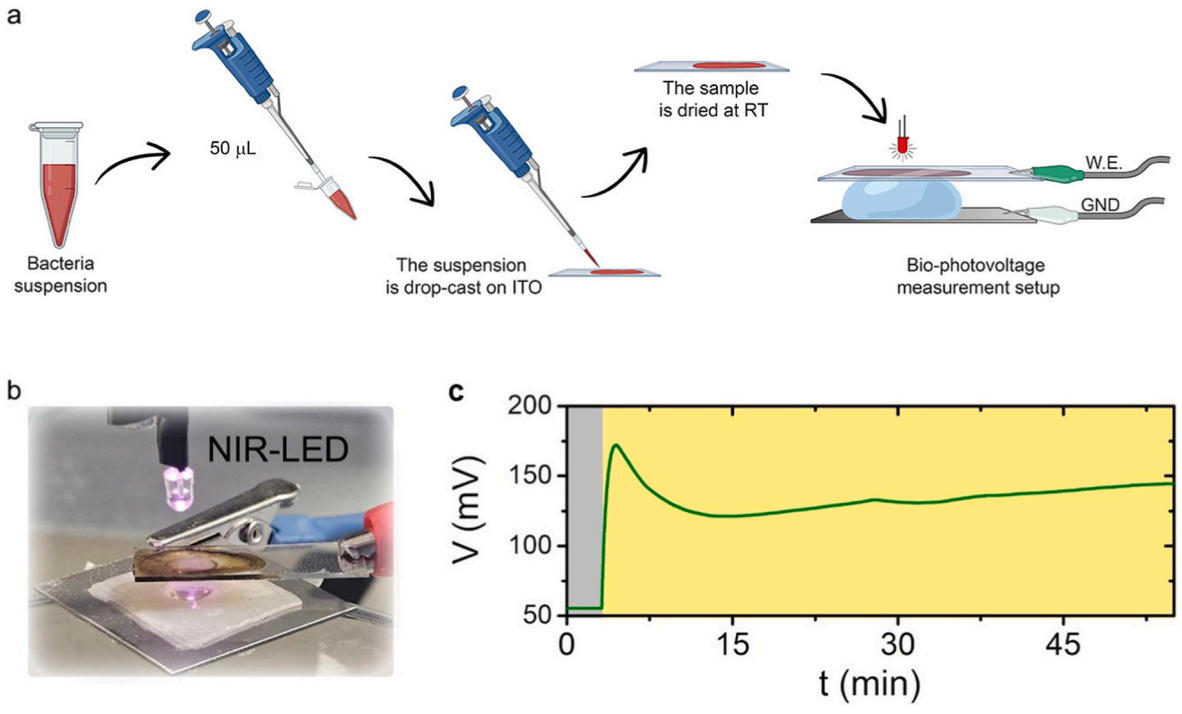

Fig. 1. a. Process flow of bio-hybrid electrode fabrication and characterization; **b.** Picture of the bio-photovoltage measurement setup, showing the NIR-LED (top), the bio-hybrid photo-sensitive electrode made of bacterial cells on ITO working electrode, and the Pt counter-electrode, with a polymeric pool for electrolyte confinement; **b.** Chronopotentiometry showing the voltage recorded at the working electrode with 2.4.1 upon NIR illumination. Grey and yellow shaded areas indicate LED OFF and LED ON periods, respectively.

isolated reaction centers, aggregated reaction centers, and microalgae.

3.2. Photovoltage time-dependent evolution

Time evolution of photovoltage generation was assessed in slow and fast cycling conditions, as detailed in the Methods, hereafter terms sNIR (Fig. 2a) and fNIR (Fig. 2b), respectively. Fig. 2a shows four subsequent sNIR cycles, yielding an average positive voltage variation ΔV as high as 57.4 ± 8.2 mV, that reverts upon illumination switch-off. This response is assimilated to four single output voltages (as that of Fig. 1b), superimposed to an exponentially increasing envelope. In fNIR cycling condition (Fig. 2b), the positive voltage variation was lower (ΔV = 34.02 (±9.71) mV). To compare performances of bio-hybrid photoelectrodes obtained from different batches of bacterial suspension, it is useful to define a parameter, Ξ. Ξ is defined as the ratio between the generated photovoltage, expressed in mV, and the bacterial concentration, expressed in colony-forming units (CFU) per unit volume (see Experimental section). In sNIR conditions, Ξ remaines unchanged at 1.76 (±0.47) × 10^{-12} mV mL CFU^{-1} upon cycling (Fig. 2c). On the contrary, under fNIR conditions, Ξ decreases during subsequent cycles, starting from 3.16(±1.12) × 10^{-12} mV mL CFU^{-1} down to a constant value of 1.78(±0.08) × 10^{-12} mV mL CFU^{-1} from the third cycle on (Fig. 2d).

A constant and predictable photovoltage allows us to envision a family of symbiotic bio/hybrid architectures for sustainable energy production. The capability to generate and sustain a potential difference strongly depends on the duration of light/dark cycles. The different responses stem from the device plasticity, borrowing a terminology proper of neuromorphic electronics to indicate the time-varying output response characteristic of the magnitude and frequency of the input stimulus. Indeed, the phenomenon reported in Fig. 2a and b can be assimilated to the extensively studied paired-pulse plasticity (Keene et al., 2021) in neuromorphic architectures, where the circuit responds to repeated voltage pulses (the input stimulus) with current spikes whose amplitude either decreases (depressing behavior) or increases (facilitating behavior). The characteristic timescales of the output spikes depend on electrolyte composition, device architecture and operational parameters. The input signal features that determine the paired-pulse plasticity are amplitude, frequency, number of pulses, and inter-stimulation interval (ISI), *i.e.* the time interval between consecutive pulses (Gkoupidenis et al., 2015; Rondelli et al., 2023).

In our photovoltage experiment, the input signal is the sequence of light/dark cycles and the elicited photovoltage is the output response. As in neuromorphic devices, two ISI-related responses can be observed in the case of bacterial cells. When the ISI between two consecutive light pulses is longer than the characteristic timescale of the device (as in sNIR condition), the system can fully relax to its dark state (baseline) after the first stimulation and before the second pulse. The output amplitude is, therefore, maintained for the subsequent sNIR cycling as in Fig. 2c. When the ISI is shorter than this characteristic time (as in fNIR condition), the second pulse will occur during the relaxation phase of the system, resulting in a memory effect (*i.e.* a positive shift of the baseline) that is maintained upon cycling and eventually leads to a final

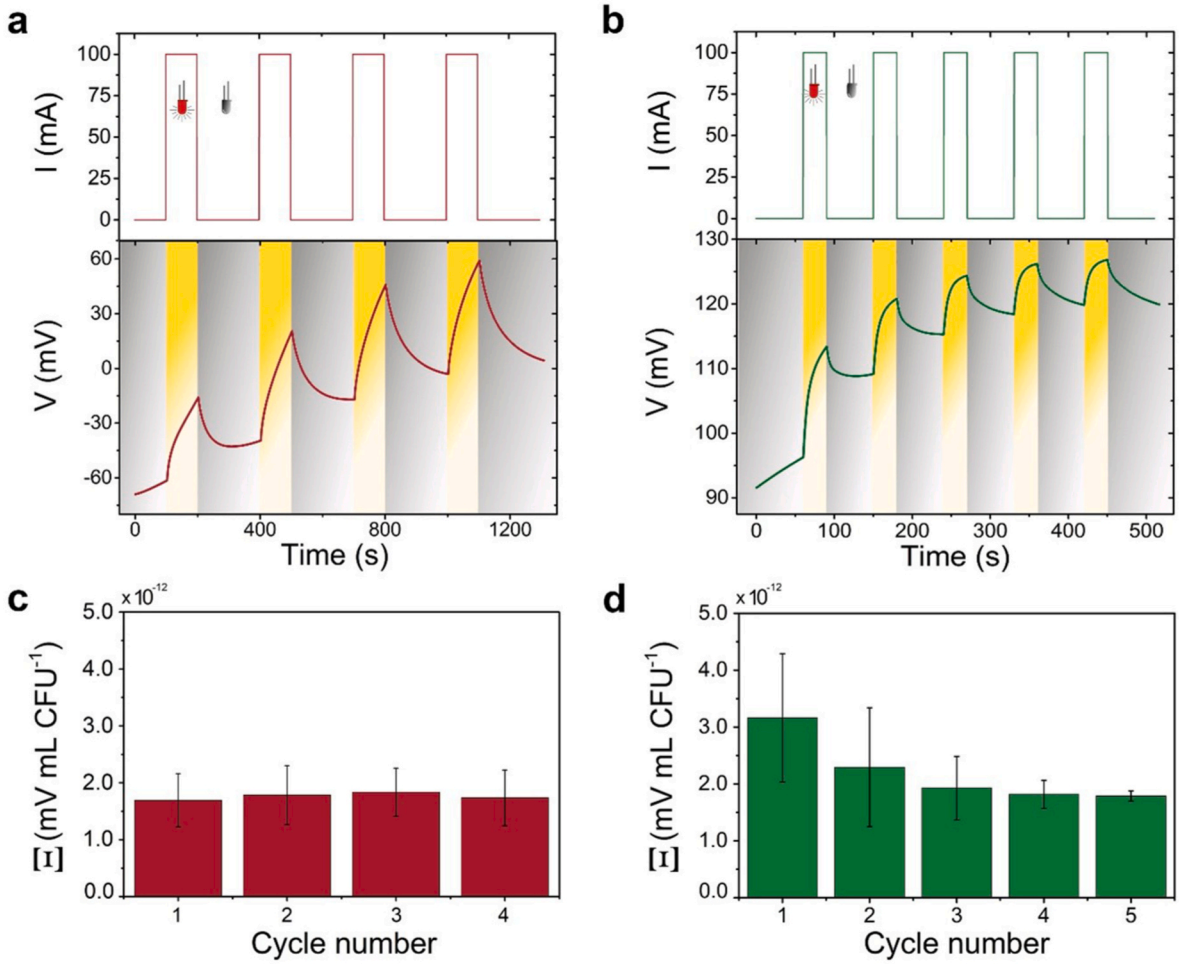

Fig. 2. a. sNIR (100 s light/200 s dark) and **b.** fNIR (30 s light/60 s dark) top, lighting cycles profiles, expressed as source current (I) vs time; bottom, respective representative chronopotentiometry plots as output photovoltage (V) vs time obtained with wild-type bacterial cells. Grey and yellow shaded areas indicate LED OFF and LED ON periods, respectively. **c-d.** Cycle evolution of the parameter Ξ over four cycles upon (c) sNIR and (d) fNIR lighting cycles. (n = 3, mean ± SD).

equilibrium state (a new baseline plateau), on which a constant output amplitude is produced at the subsequent fNIR cycles, with a magnitude smaller than the one obtained in sNIR. Understanding and optimizing the lighting conditions and the light/dark cycles is hence crucial for any technological integration harnessing the full potential of photosynthetic microorganisms.

Charge and discharge profile (expressed as Ξ vs time trends averaged over cycles) can be quantitatively described by either one or two exponential time constants (τ_1 and τ_2) and their respective signal amplitudes ($\Delta\Xi_1$ and $\Delta\Xi_2$). The parameters τ and ΔΞ are summarized in Table 1. In sNIR, the photovoltage rises according to a bi-exponential trend (Fig. 3a) and decays following a mono-exponential trend (Fig. 3b). In fNIR, the photovoltage grows according to a mono-exponential trend with a τ comparable to the τ_1 of sNIR cycles (Fig. 3c) while the relaxation profile obeys a bi-exponential trend (Fig. 3d).

The time evolution of the photogenerated signals in both lighting conditions closely resembles what happens in neuromorphic systems exhibiting paired-pulse plasticity under different ISI. In sNIR - ISI longer than the device's characteristic time - the photovoltage rise can be described by two build-up processes, namely an "onset" (corresponding to τ_1) and an "evolution" (corresponding to τ_2). When the light stimulus is removed the system decays with a single relaxation time constant (τ_r). In fNIR - ISI shorter than the device's characteristic time - the rise is mono-exponential (i.e. described by a single τ_1), while the decay after light switch-off is bi-exponential and described by the relaxation timescales (τ_{r1} and τ_{r2}). Accordingly, photovoltages elicited by sNIR and fNIR cycling give rise to two different relaxation profiles, with the two relaxation pathways being mutually exclusive.

3.3. The role of carotenoids

Long-term stability and feature reproducibility were assessed upon sNIR cycles also using the carotenoidless mutant strain R26. In the UV–Visible–NIR absorption spectroscopy of R26 strain (Fig. S1), no carotenoid peaks were observed, and the characteristic peak of the sole RC-LH1 complex antenna appears at 865 nm (Cogdell et al., 1997) with an additional peak at 590 nm.

On ITO electrode (Fig. 4a), R26 elicits a positive constant ΔV as high as 33 ± 3 mV throughout four consecutive cycles. With $\Xi = 6.1(\pm0.2) \times 10^{-12}$ mV mL CFU^{-1} (Fig. 4b). This value is almost three times higher than that of wild-type 2.4.1 cells (Fig. 2c). The charge and discharge profiles (Fig. 4c and d) recorded for the R26 mutant strain follow comparable trends with those found in 2.4.1 (Fig. 3) (data are reported in Table 2).

The enhanced performance of R26, namely a sensibly higher Ξ and a constant voltage output under sNIR conditions can be ascribed to the lack of carotenoids in the photosynthetic apparatus (Cogdell and Crofts, 1978; Cogdell et al., 1997). This is counterintuitive, since the overall optical cross section of the photosynthetic apparatus is higher in the wild type than in the mutant strains that lack carotenoids, and hence are not capable of correctly assembling the accessory light harvesting complex LH2. As a result, one would expect that mutant cells should underperform compared to the wild type in generating photovoltage. This is not the case of our setup since, under the experimental conditions used here, the illumination saturates the whole photosynthetic apparatus, hence both strains work at their highest conversion capability.

Table 1
Fit parameters for the photovoltage evolution – wild-type cells.

Light/dark fitting function	τ (s)	ΔΞ (mV mL CFU^{-1})
sNIR - Slow condition (100 s light/200 s dark)		
light:	**light:**	**light:**
bi-exponential	$\tau_1 = 7.21(\pm0.07)$	$\Delta\Xi_1 = 3.05(\pm0.02) \times 10^{-13}$
	$\tau_2 = 159(\pm1)$	$\Delta\Xi_2 = 3.08(\pm0.02) \times 10^{-12}$
dark:	**dark:**	**dark:**
exponential	$\tau_r = 45.7(\pm0.1)$	$\Delta\Xi_1 = 1.398(\pm0.001) \times 10^{-12}$
fNIR - Fast condition (30 s light/60 s dark)		
light:	**light:**	**light**:
exponential	$\tau_1 = 8.97(\pm0.09)$	$\Delta\Xi_1 = 3.23(\pm0.02) \times 10^{-12}$
dark:	**dark:**	**dark:**
bi-exponential	$\tau_{r1} = 2.530\ (\pm0.005)$	$\Delta\Xi_1 = 6.68(\pm0.01) \times 10^{-13}$
	$\tau_{r2} = 59.6(\pm0.1)$	$\Delta\Xi_2 = 2.223(\pm0.002) \times 10^{-12}$

The enhanced performance observed in the carotenoid-deficient mutant is primarily attributed to a fundamental change in the photophysical management of excitation energy. Carotenoids primarily broaden the absorption spectrum of the photosynthetic apparatus by transferring singlet excitation energy to the bacteriochlorophyll molecules within the antenna complexes—an energy transfer that occurs on the femtosecond timescale through excitonic coupling. They also act as highly efficient quenchers of the long-lived triplet state of bacteriochlorophyll (^{3}BChl*), and reactive oxygen species, like singlet oxygen during the early photophysical events that take place in the photosynthetic reaction center under the conditions of excess light. In wild-type cells, this quenching process provides an effective photoprotective mechanism, dissipating excess excitation energy non-radiatively and thereby preventing the formation of reactive oxygen species and photooxidative damage within the reaction center. This dual function is essential for safeguarding against excessive light absorption by antenna complexes, which can overwhelm the RC's ability to carry out the photochemical reactions (Ruban, 2016). In the mutant, the absence of carotenoids and the subsequent lack of their photoprotective role, impairs this triplet-state quenching, resulting in a higher fraction of absorbed excitation energy remaining available for charge separation at the RC. Consequently, the photosynthetic electron transport chain operates with an increased steady-state electron flux. While the risk of photo-oxidative stress (which would be evident over very long observation periods) increases, in the measured time scale, their absence, enables an enhanced photosynthetic activity of the mutant strain compared to the wild-type strain since no light dissipation mechanism is present in R26 (Cogdell and Crofts, 1978), at the price of a lowered stability. Since the photovoltage signal recorded in whole cells reflects the kinetic efficiency and overall throughput of the photosynthetic electron transport chain, this enhanced electron flux directly accounts for the higher and more stable photovoltage observed under the specific sNIR illumination conditions of our experiments. This evidence, far from being conclusive, hints at the existence of a trade-off between high performance and long-term stability when aiming at bio-hybrid symbiotic architectures, thus highlighting the crucial importance of selecting the appropriate bacterial strain for the desired application (e.g., choosing R26 mutant for higher-power/shorter-term applications and 2.4.1 for lower-power/longer-term ones).

3.4. The role of pH

The performances of the two bacterial strains are also compared in response to variation of the electrolyte pH, under fNIR cycling conditions (Fig. 5). The recorded <Ξ> is $1.96(\pm0.34) \times 10^{-12}$ mV mL CFU^{-1} at pH 7 (Figs. 5a), $3.18(\pm0.52) \times 10^{-12}$ mV mL CFU^{-1} at pH 8 (Figs. 5c) and $4.43(\pm0.23) \times 10^{-12}$ mV mL CFU^{-1} at pH 9 for the wild-type strain (Fig. 5e) averaged over four consecutive illumination cycles. For the mutant strain, <Ξ> is $3.99(\pm0.71) \times 10^{-12}$ mV mL CFU^{-1} at pH 7 (Figs. 5b), $7.68(\pm0.43) \times 10^{-12}$ mV mL CFU^{-1} at pH 8 (Figs. 5d) and $6.99(\pm0.51) \times 10^{-12}$ mV mL CFU^{-1} at pH 9 (Fig. 5f) averaged over four cycles.

It is worth noticing that, as the pH increases, the baseline voltage is shifted towards lower potentials, hinting at a more negative chemical potential of the solution. In the proposed architecture, an increase of the generated photovoltage - and a subsequent Ξ increase - are recorded while moving towards alkaline pH values, as summarized in Table 3. The

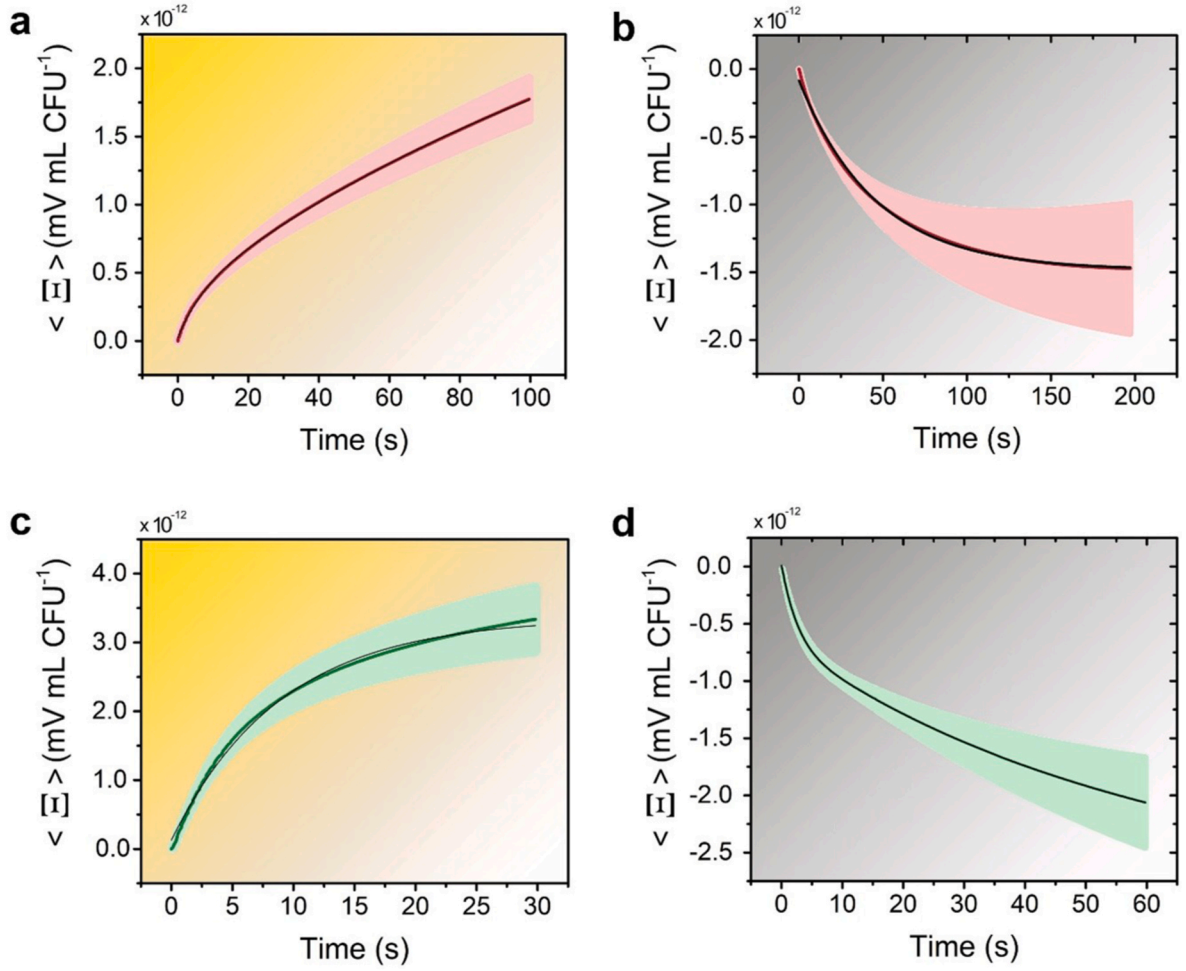

Fig. 3. **a.** Charge (upon illumination) and **b.** Discharge (in the dark) profiles, <Ξ> vs time, generated by wild-type strain in slow lighting conditions sNIR averaged over 4 cycles. **c.** Charge and **d.** Discharge profiles, <Ξ> vs time generated by wild-type strain in fast lighting conditions averaged over 4 cycles. Black line represents the fitted curves and shadows represent the standard deviation (n = 3) in all graphs. Grey and yellow shaded areas indicate LED OFF and LED ON periods, respectively.

Ξ, at different pH and from different cycles, in the case of the wild-type and of the mutant strains, are shown in Fig. 5g and h respectively.

By varying the pH and, consequently, the chemical potential of the solution, a constant response is observed only for R26 and after the first cycle. The photovoltage build-up process at different pH confirms the plasticity of the system due to ionic environmental conditions (Table 3).

For the wildtype, the time evolution follows the previously described trend at pH 7, confirming that photovoltage build-up is not completed during fNIR illumination. Increasing the alkalinity, this process becomes bi-exponential during the illuminated phase. A bi-exponential relaxation rate can be observed upon ceasing illumination at pH 8 and 9, respectively. The overall effect of alkalization on photovoltage generation is an increase of the stored energy during the illuminated phase. Upon pH increase, the threshold build-up time can be reached, as confirmed by the onset and evolution time constants, and the discharge profiles become faster.

The exponential build-up trend, with slower τ_1 upon pH increase, confirms the enhancement in energy storage for the mutant strain even under fNIR conditions, where the brief light exposure is insufficient to build-up a stable voltage at physiological pH. The lack of carotenoids that push forward the system light saturation, slows down the discharge process upon pH increase, yielding higher photovoltage generation efficiency. Interestingly, long-term baseline modulation is achieved with 2.4.1 strain (Fig. 5a–c-e), hinting at a capability of the wild-type strain to permanently alter the chemical potential of the electrolyte, which is absent in the carotenoid-less mutant (Fig. 5b–d-f).

3.5. *Mechanism hypothesis*

The primary goal of the light-driven electron transfer in purple bacteria is to establish a proton gradient across the inner membrane, which is exploited by ATP-synthase to generate adenosine triphosphate (ATP) for bacterial metabolism. This photoinduced proton motion, which consists of an outflow of protons from the cytoplasm to the periplasm (useful for metabolism) and, upon continuous illumination, in an outflow towards the extracellular environment (useful to maintain a constant pH in the periplasmic space), might provide a rationale for the observed photovoltage generation. The photovoltage recorded in our system reflects the overall metabolic throughput of the fully functional photosynthetic electron transport chain. Notably, in a photovoltage generation experiment, the adventitious interfacial electron transfer occurring through the cell envelope toward the conductive ITO substrate might be regarded as a parasitic phenomenon, since it would not contribute to photovoltage generation (*i.e.* charge build-up) but would rather result in an additional discharge pathway. This might explain why the mutant R26 is more efficient in photovoltage generation than the wild type strain, albeit featuring a less performing photosynthetic unit.

It is possible to hypothesize that protons transported to the extracellular environment are responsible for the electrode potential shift.

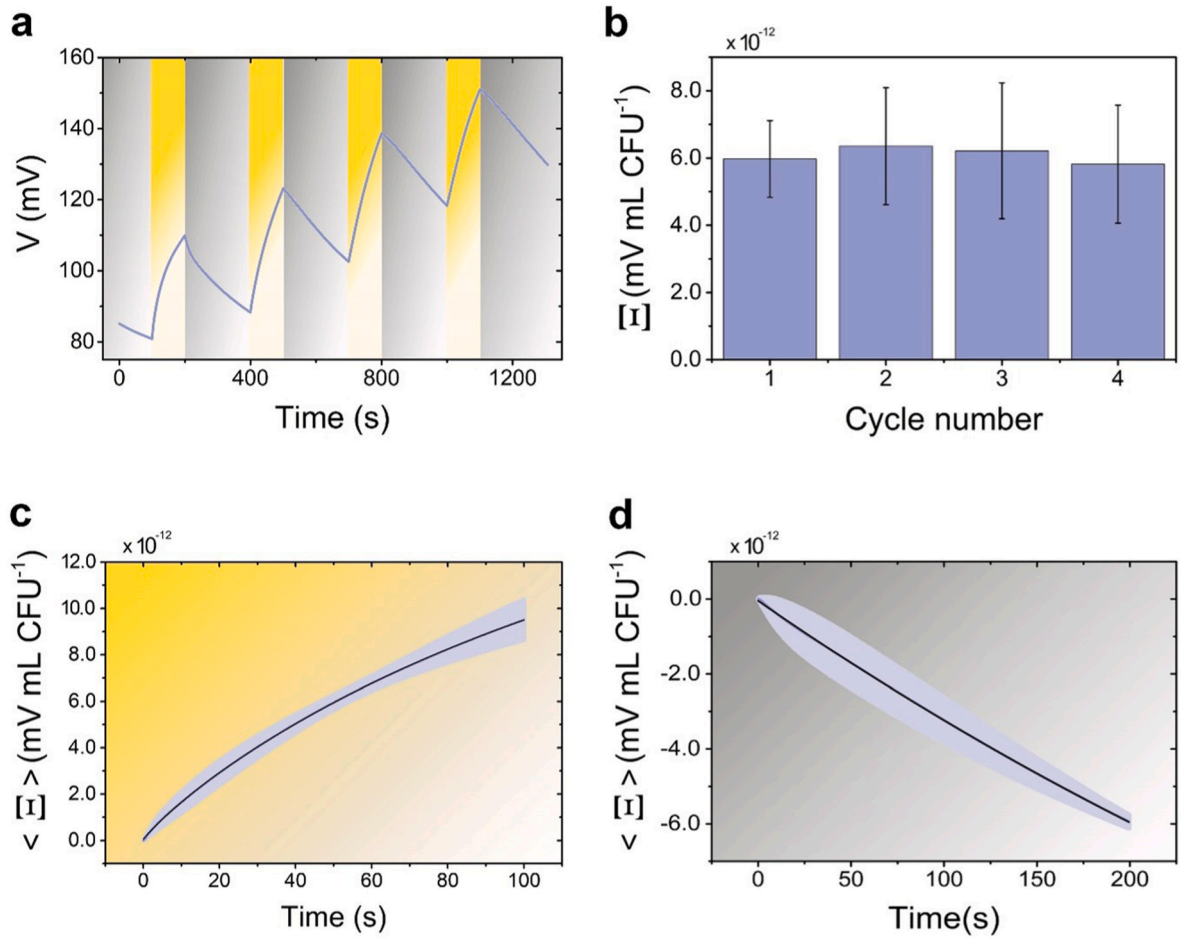

Fig. 4. **a.** Representative chronopotentiometry, acquired voltage (V) versus time, of the photovoltage generated with *R. sphaeroides* carotenoid-less mutant strain R26 upon sNIR cycles. **b.** Parameter Ξ over four cycles in sNIR condition (n = 3, mean ± SD). **c.** Charge and **d.** Discharge profiles (<Ξ> vs time) generated by mutant strain in sNIR conditions over 4 cycles (n = 3, mean ± SD). Grey and yellow shaded areas indicate LED OFF and LED ON periods, respectively.

Table 2
Fit parameters for the photovoltage evolution - carotenoid-less mutants.

Light/dark fitting function	τ (s)	ΔΞ (mV mL CFU^{-1})
sNIR - Slow condition (100 s light/200 s dark)		
light:	**light:**	**light:**
bi-exponential	$\tau_1 = 9.8(\pm 0.2)$	$\Delta\Xi_1 = 5.1(\pm 0.1) \times 10^{-13}$
	$\tau_2 = 121.3(\pm 0.6)$	$\Delta\Xi_2 = 1.58(\pm 0.01) \times 10^{-11}$
dark:	**dark:**	**dark:**
exponential	$\tau_r = 643(\pm 3)$	$\Delta\Xi_1 = 2.21(\pm 0.01) \times 10^{-11}$

First, the positive voltage shifts that are always obtained upon illumination strongly suggest an accumulation of positive charges in the proximity of the electrode. This scenario is compatible with a consistent and photosynthetically sustained proton outflow. Second, the smaller magnitude of the photovoltage in 2.4.1 reflects the optimized nature of wild-type metabolism to thrive under prolonged light exposition compared to R26. Indeed, the recorded higher photovoltage and lower stability of mutants can reflect the absence of control mechanisms, giving rise to uncontrolled outward proton translocation upon light overstimulation. The behavior of R26, although technologically interesting, hints to an impaired capability of photosynthetic cells to finely regulate proton motion, as a consequence of the absence of photoprotective carotenoids, making this strain more affected than 2.4.1 by all the investigated environmental conditions. Third, proton translocation towards the extracellular space is a parasitic phenomenon, which regards solely protons exceeding the metabolic needs of the organism, which must occur at longer timescales, such as those of photovoltage build-up. The results on pH-dependence of the photogenerated voltage support this hypothesis, since an increase of the extracellular pH, corresponding to an increase of pH in the electrolyte, leads to an increased driving force for the outwards proton translocation. It is important to stress that, although these evidence strongly support the existence of a link between proton transport and photovoltage generation, additional investigation to provide direct mechanistic demonstration of this link is still needed (e.g., by using pH - sensitive dye or membrane potential sensors).

3.6. *Application of the biohybrid electrode: LEGOT and symbiotic power cell*

To exploit the extensively investigated photovoltage generation capability of whole metabolically active bacteria, it is necessary to engineer bio/hybrid architectures that integrate an electrolyte environment suitable for bacterial life in their functional principles. Here, we show two demonstrators of this concept: a Light-modulated Electrolyte-Gated Organic Transistor - LEGOT - based on a poly-3,4-ethylenedioxythiophene:poly-stirene sulfonate (PEDOT:PSS) conductive channel (Di Lauro et al., 2019, 2020a), and a power cell in which the sole functional element is the bacterial suspension.

In the LEGOT, the photoactive electrode was used as a gate electrode (G), immersed in the working electrolyte which also contacts the PEDOT:PSS film between the source (S) and drain (D) terminals. Fig. 6a shows the circuit schematics and the conceptual 3D models of the

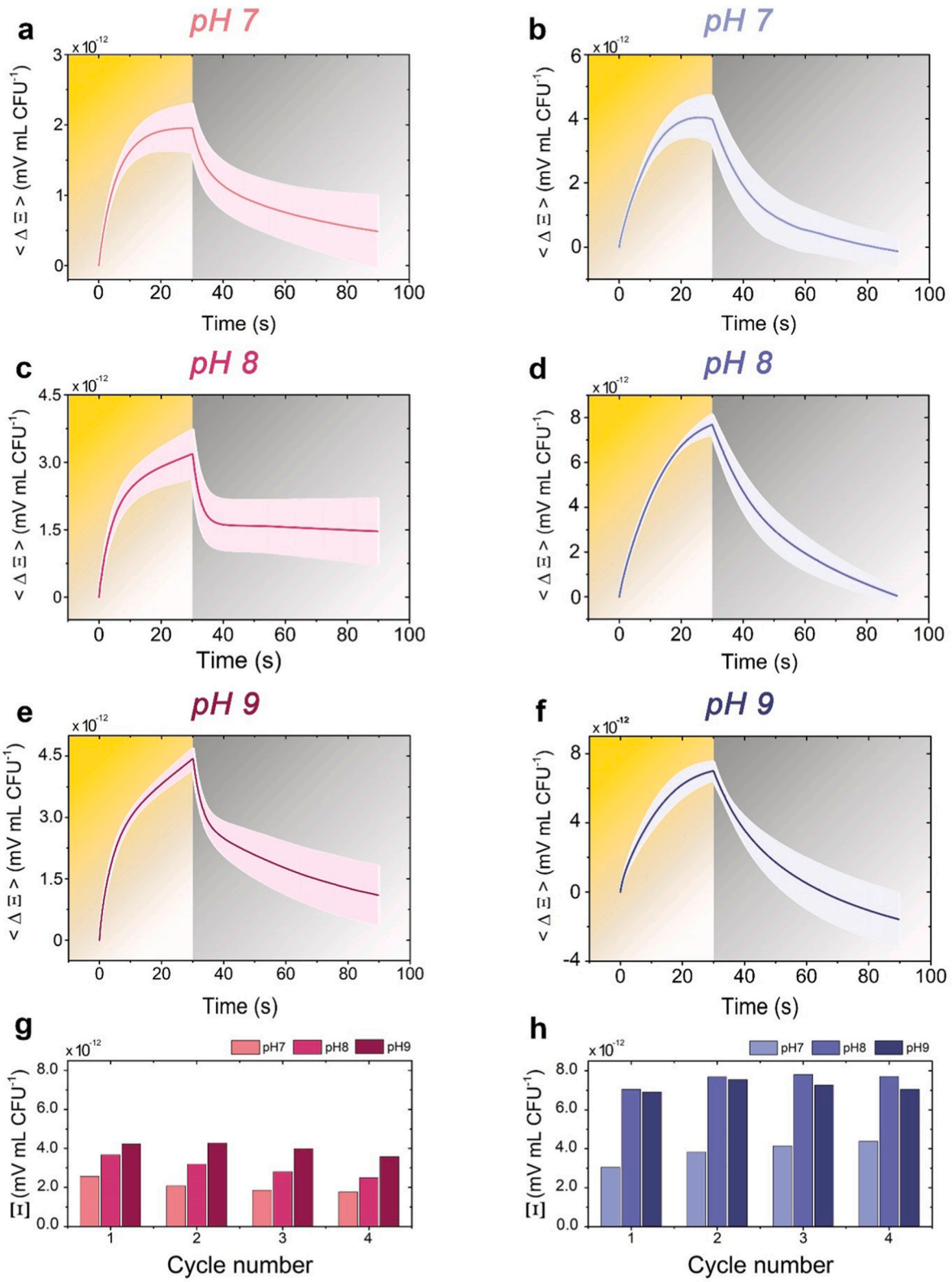

Fig. 5. a-c-e. Time evolution of the averaged Ξ recorded using bacterial cells of the wild-type strain of *R. sphaeroides* at **a.** pH 7, **c.** pH 8 and **e.** pH 9. The light pink shadow represents the standard deviation over four cycles. **b-d-f.** Time evolution of the averaged Ξ recorded using mutant strain at **b.** pH 7, **d.** pH 8 and **f.** pH 9. The light violet shadow represents the standard deviation over four cycles. All the measurements are carried out in fNIR conditions (30 s light/60 s dark). Grey and yellow shaded areas indicate LED OFF and LED ON periods, respectively; **g-h. Dependency of** Ξ Amplitude of the generated photovoltage with **g**. Wild-type and **h.** Mutant strain at different pH values upon cycling.

Table 3
pH-dependence of photovoltagebuild-up kinetics.

pH	Light/dark fitting function	τ (s)	ΔΞ (mV mL CFU^{-1})
Wild type bacteria			
7	**light:**	**light:**	**light:**
	exponential	$\tau_1 = 5.69\ (\pm0.01)$	$\Delta\Xi_1 = 1.944\ (\pm0.002) \times 10^{-12}$
	dark:	**dark:**	**dark:**
	bi-exponential	$\tau_{r1} = 3.77\ (\pm0.02)$	$\Delta\Xi_1 = 5.71\ (\pm0.02) \times 10^{-13}$
		$\tau_{r2} = 39.23\ (\pm0.21)$	$\Delta\Xi_2 = 1.071\ (\pm0.001) \times 10^{-12}$
8	**light:**	**light:**	**light:**
	bi-exponential	$\tau_1 = 3.91\ (\pm0.03)$	$\Delta\Xi_1 = 2.09\ (\pm0.02) \times 10^{-12}$
		$\tau_2 = 42.3\ (\pm2.8)$	$\Delta\Xi_2 = 2.07(\pm0.06) \times 10^{-12}$
	dark:	**dark:**	**dark:**
	exponential	$\tau_r = 2.75\ (\pm0.04)$	$\Delta\Xi_1 = 1.49\ (\pm0.02) \times 10^{-12}$
9	**light:**	**light:**	**light:**
	bi-exponential	$\tau_1 = 3.59\ (\pm0.04)$	$\Delta\Xi_1 = 2.26(\pm0.02) \times 10^{-12}$
		$\tau_2 = 67.8\ (\pm5.9)$	$\Delta\Xi_2 = 5.8(\pm0.3) \times 10^{-12}$
	dark:	**dark:**	**dark:**
	bi-exponential	$\tau_{r1} = 2.45\ (\pm0.01)$	$\Delta\Xi_1 = 1.408\ (\pm0.002) \times 10^{-12}$
		$\tau_{r2} = 52.17\ (\pm0.23)$	$\Delta\Xi_2 = 2.683(\pm0.005) \times 10^{-12}$
Mutant bacteria			
7	**light:**	**light:**	**light:**
	exponential	$\tau_1 = 8.74\ (\pm0.08)$	$\Delta\Xi_1 = 4.36\ (\pm0.01) \times 10^{-12}$
	dark:	**dark:**	**dark:**
	exponential	$\tau_r = 15.2\ (\pm0.1)$	$\Delta\Xi_1 = 3.88\ (\pm0.01) \times 10^{-12}$
8	**light:**	**light:**	**light:**
	exponential	$\tau_1 = 14.03\ (\pm0.05)$	$\Delta\Xi_1 = 8.73\ (\pm0.01) \times 10^{-12}$
	dark:	**dark:**	**dark:**
	exponential	$\tau_r = 24.37\ (\pm0.17)$	$\Delta\Xi_1 = 7.82\ (\pm0.02) \times 10^{-12}$
9	**light:**	**light:**	**light:**
	exponential	$\tau_1 = 12.99\ (\pm0.06)$	$\Delta\Xi_1 = 7.58\ (\pm0.01) \times 10^{-12}$
	dark:	**dark:**	**dark:**
	bi-exponential	$\tau_{r1} = 8.62\ (\pm0.05)$	$\Delta\Xi_1 = 2.49\ (\pm0.01) \times 10^{-12}$
		$\tau_{r2} = 43.29\ (\pm0.23)$	$\Delta\Xi_2 = 7.984\ (\pm0.006) \times 10^{-12}$

LEGOT, as well as the chronoamperogram used for driving the light source in the NIR-illumination experiment, with cycles of 30 s light/60 s dark. Transfer characteristics of these devices, operated with bio-hybrid gate electrodes, showed the typical depletion-mode response of PEDOT:PSS-based EGOTs (Fig. 6b), with transconductance values in the 3–5 mS range. Current modulation upon illumination was evaluated in a chronoamperometry experiment in which both V_{DS} and V_{GS} are kept fixed, at −0.7 V and 0.0 V, respectively (Fig. 6c). In this configuration, proton outflow cannot result in an adjustment of the electrode potential (which is forced to be 0.0 V with respect to the grounded source terminal), hence the effect of light absorption is to increase the effective capacitance of the gate/electrolyte interface, which ultimately results into a larger (more negative) p-type current in the PEDOT:PSS channel. In this example, the average light-induced current increase is as high as 122.5 ± 12.6 μA, which is the same that would be induced by a ~30 mV voltage pulse at the gate electrode in the same architecture.

The final and simplest demonstrator of the technological exploitability of the herein presented voltage generation is a power cell obtained by placing two identical stainless-steel electrodes directly in the wild-type bacterial suspension, and measuring the bias between them upon exposing the cell to direct sunlight illumination (Fig. 6d). This configuration, far from ideality both in terms of geometry and of incident wavelength, is investigated as a benchmark of in-field application. Fig. 6e shows the resulting chronopotentiogram, achieved by physically displacing the cell between a shaded and a sunny position on the laboratory bench, with cycles of roughly 60 s. Despite the coarseness of the method, it is possible to harvest direct sunlight and to generate and sustain $<\Delta V> = 2.98 \pm 0.17$ mV with good reproducibility over the investigated timespan. This performance, rather poor *per se* if compared to architectures relying on close packing of oriented reaction centers on electrodes, represents a huge leap with respect to the state of the art in terms of in-field deployability, since it enables direct harvesting of solar energy without requiring surface chemistry nor protein isolation and purification.

4. Conclusions

The use of whole metabolically active bacteria provides an inherently robust and potentially self-renewable platform for harvesting solar energy by means of natural photosynthetic apparata. This non-faradaic photoresponse, here extensively investigated, can be modulated either via genetic engineering on the bacterial strains or by altering the chemo-physical variables of the working electrolyte/culture medium. To the

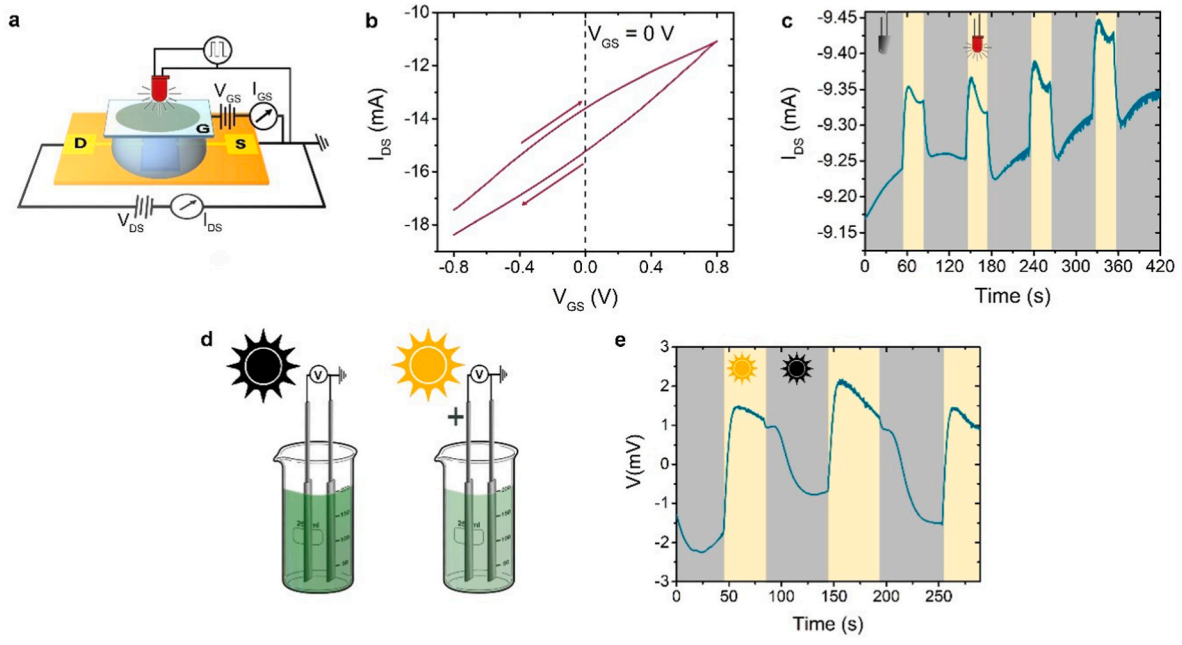

Fig. 6. a. Sketch of LEGOT connection scheme. b. Transfer curve of the LEGOT ($V_{DS} = -0.7$ V, V_{GS} linearly scanned between −0.8 V and 0.8 V). **c.** I_{DS} versus t plot of LEGOT, with ITO electrodes covered with wild type bacteria by driving the LEGOT device with V_{GS} equal to 0 V. Grey and yellow shaded areas indicate LED OFF and LED ON periods, respectively. **d.** Sketch of the experimental setup for photo-voltage generation measurement under sunlight illumination. **e.** Photovoltage generated during sun-shadow exposure. Grey and yellow shaded areas indicate periods of exposure to shadow and to sunlight, respectively.

best of our knowledge, no previous studies have reported photovoltage generation from whole photosynthetic bacterial cells, and thus a direct comparison within this framework is not available. The advantages of our platform lie in its ease of fabrication, the absence of protein purification steps typical of systems based on isolated photosynthetic complexes, and the inherent self-renewability of the active bio-layer. Compared with algal-based systems, it also offers simpler, faster, and more efficient culturing and handling. In contrast, artificial photosynthetic systems—though technologically advanced—raise concerns regarding sustainability; consequently, the conceptual foundation of this work aligns with the broader effort to develop biohybrid architectures as viable and sustainable alternatives. This approach represents a first step towards the symbiotic integration of photosynthetic bacteria and artificial technology, as testified by two technological demonstrators. Ultimately, this work presents routes to take advantage of a physiological stress-protection mechanism of photosynthetic bacteria, namely the translocation of protons towards the extracellular space, to attain technologically exploitable bias. Importantly, photovoltage generation and stabilization is not harmful for the biolayer while, at the same time, is extremely useful for energy conversion. Future research efforts, building on the results herein presented, obtained under tightly controlled laboratory conditions, shall pursue the achievement of long-term stability over repetitive cycling, as well as effective translation to real-world operational scenarios, where temperature variations may alter the rate of photosynthetic electron transport and membrane fluidity, while humidity can affect biofilm hydration and charge transfer at the cell–electrode interface. Additionally, a finer characterization of light-intensity modulation—using alternative waveforms such as sine or triangular inputs to dynamically vary the excitation current—represents an interesting direction for future studies. Since *R. sphaeroides* exhibits a pronounced physiological response to changes in light intensity, exploring such modulation schemes could yield deeper insights into the interplay between cellular photodynamics and device performance. Accordingly, these proof-of-concept results have the potential to foster extensive additional research in the field of bio-hybrid device engineering, aiming at novel, symbiotic and sustainable tools for the green and circular energy market of the future.

CRediT authorship contribution statement

Rossella Labarile: Writing – original draft, Investigation, Formal analysis, Data curation. **Anna De Salvo:** Writing – original draft, Investigation, Formal analysis, Data curation. **Federico Rondelli:** Investigation, Formal analysis. **Maria Michela Giangregorio:** Visualization, Investigation, Data curation. **Michele Di Lauro:** Writing – review & editing, Visualization, Methodology, Conceptualization. **Massimo Trotta:** Writing – review & editing, Visualization, Methodology, Conceptualization. **Gianluca Maria Farinola:** Supervision, Funding acquisition. **Fabio Biscarini:** Supervision, Funding acquisition.

Declaration of competing interest

The authors declare that they have no known competing financial interests or personal relationships that could have appeared to influence the work reported in this paper.

Acknowledgements

R.L. and A.D.S. contributed equally to this work. All authors acknowledge the project PrinPNRR2022—P20225NFS4 (PhOLcs—-Photosynthesis for Organic Light-Powered Electronics). G.M.F. and F.B. contributed equally to this work.

Appendix A. Supplementary data

Supplementary data to this article can be found online at https://doi.org/10.1016/j.bios.2025.118260.

Data availability

Data will be made available on request.

References

Ahmadi, A., Khoshfetrat, S.M., Kabiri, S., Fotouhi, L., Dorraji, P.S., Omidfar, K., 2021. Impedimetric paper-based enzymatic biosensor using electrospun Cellulose Acetate Nanofiber and reduced graphene oxide for detection of glucose from whole blood. IEEE Sens. J. 21 (7), 9210–9217.

Berry, E.A., Huang, L.S., Saechao, L.K., Pon, N.G., Valkova-Valchanova, M., Daldal, F., 2004. X-ray structure of Rhodobacter capsulatus cytochrome bc(1): comparison with its mitochondrial and chloroplast counterparts. Photosynth. Res. 81, 251–275.

Brown, K.A., King, P.W., 2020. Coupling biology to synthetic nanomaterials for semi-artificial photosynthesis. Photosynth. Res. 143 (2), 193–203.

Buccolieri, A., Italiano, F., Dell'Atti, A., Buccolieri, G., Giotta, L., Agostiano, A., Milano, F., Trotta, M., 2006. Testing the photosynthetic bacterium Rhodobacter sphaeroides as heavy metal removal tool. Ann. Chim. 96 (3–4), 195–203.

Carniello, V., Peterson, B.W., van der Mei, H.C., Busscher, H.J., 2018. Physico-chemistry from initial bacterial adhesion to surface-programmed biofilm growth. Adv. Colloid Interface Sci. 261, 1–14.

Chen, L., Chen, Z., Zhang, Y., Liu, Y., Osman, A.I., Farghali, M., Hua, J., Al-Fatesh, A., Ihara, I., Rooney, D.W., Yap, P.-S., 2023. Artificial intelligence-based solutions for climate change: a review. Environ. Chem. Lett. 21 (5), 2525–2557.

Chinipardaz, M., Khoramfar, A., Amraee, S., 2024. Green internet of things and solar energy. Environ. Sci. Pollut. Res. Int. 31 (12), 18296–18312.

Clayton, R.K., 1960. The induced synthesis of catalase in Rhodopseudomonas spheroides. Biochim. Biophys. Acta 37, 503–512.

Clayton, R.K., Smith, C., 1960. Rhodopseudomonas spheroides: high catalase and blue-green double mutants. Biochem. Biophys. Res. Commun. 3, 143–145.

Cogdell, R.J., Crofts, A.R., 1978. Analysis of the pigment content of an antenna pigment-protein complex from three strains of Rhodopseudomonas sphaeroides. Biochim. Biophys. Acta 502 (3), 409–416.

Cogdell, R.J., Isaacs, N.W., Freer, A.A., Arrelano, J., Howard, T.D., Papiz, M.Z., Hawthornthwaite-Lawless, A.M., Prince, S., 1997. The structure and function of the LH2 (B800–850) complex from the purple photosynthetic bacterium Rhodopseudomonas acidophila strain 10050. Prog. Biophys. Mol. Biol. 68 (1), 1–27.

Cooley, J.W.L., D, W., Daldal, F., 2009. Across membrane communication between the Q (o) and q(i) active sites of cytochrome bc(1). Biochemistry 48, 1888–1899.

Csiki, R., Drieschner, S., Lyuleeva, A., Cattani-Scholz, A., Stutzmann, M., Garrido, J.A., 2018. Photocurrent generation of biohybrid systems based on bacterial reaction centers and graphene electrodes. Diam. Relat. Mater. 89, 286–292.

Das, R., Kiley, P.J., Segal, M., Norville, J., Yu, A.A., Wang, L., Trammell, S.A., Reddick, L. E., Kumar, R., Stellacci, F., Lebedev, N., Schnur, J., Bruce, B.D., Zhang, S., Baldo, M., 2004. Integration of photosynthetic protein molecular complexes in solid-state electronic devices. Nano Lett. 4, 1079–1083.

Di Lauro, M., Buscemi, G., Bianchi, M., De Salvo, A., Berto, M., Carli, S., Farinola, G.M., Fadiga, L., Biscarini, F., Trotta, M., 2020a. Photovoltage generation in enzymatic bio-hybrid architectures. MRS Advances 5 (18–19), 985–990.

Di Lauro, M., De Salvo, A., Sebastianella, G.C., Bianchi, M., Carli, S., Murgia, M., Fadiga, L., Biscarini, F., 2020b. Tunable short-term plasticity response in three-terminal organic neuromorphic devices. ACS Appl. Electron. Mater. 2 (7), 1849–1854.

Di Lauro, M., la Gatta, S., Bortolotti, C.A., Beni, V., Parkula, V., Drakopoulou, S., Giordani, M., Berto, M., Milano, F., Cramer, T., Murgia, M., Agostiano, A., Farinola, G.M., Trotta, M., Biscarini, F., 2019. A bacterial photosynthetic enzymatic unit modulating organic transistors with light. Adv. Electron. Mater. 6 (1).

Di Lauro, M., Zucchini, E., De Salvo, A., Delfino, E., Bianchi, M., Murgia, M., Carli, S., Biscarini, F., Fadiga, L., 2022. A novel biasing scheme of electrolyte-gated organic transistors for safe in vivo amplification of electrophysiological signals. Adv. Mater. Interfac. 9 (11).

El-Khouly, M.E., El-Mohsnawy, E., Fukuzumi, S., 2017. Solar energy conversion: from natural to artificial photosynthesis. J. Photochem. Photobiol. C Photochem. Rev. 31, 36–83.

Genitoni, M., Greco, P., Paradisi, A., Sensi, M., Berto, M., Murgia, M., Di Lauro, M., Bortolotti, C.A., Fadiga, L., Biscarini, F., 2025. Discrimination of tryptophan enantiomers at Sub-pm level by multiparametric analysis of a label-free organic immunosensor. Small Methods, e2500545.

Giordani, M., Sensi, M., Berto, M., Di Lauro, M., Bortolotti, C.A., Gomes, H.L., Zoli, M., Zerbetto, F., Fadiga, L., Biscarini, F., 2020. Neuromorphic organic devices that specifically discriminate dopamine from its metabolites by nonspecific interactions. Adv. Funct. Mater. 30 (28).

Giotta, L., Agostiano, A., Italiano, F., Milano, F., Trotta, M., 2006. Heavy metal ion influence on the photosynthetic growth of Rhodobacter sphaeroides. Chemosphere 62 (9), 1490–1499.

Gkoupidenis, P., Schaefer, N., Garlan, B., Malliaras, G.G., 2015. Neuromorphic functions in PEDOT:PSS organic electrochemical transistors. Adv Mater 27 (44), 7176–7180.

Guang-Wen, Z., Murshed, M., Siddik, A.B., Alam, M.S., Balsalobre-Lorente, D., Mahmood, H., 2022. Achieving the objectives of the 2030 sustainable development goals agenda: causalities between economic growth, environmental sustainability, financial development, and renewable energy consumption. Sustain. Dev. 31 (2), 680–697.

Hajdu, K., Balderas-Valadez, R.F., Carlino, A., Agarwal, V., Nagy, L., 2022. Porous silicon pillar structures/photosynthetic reaction centre protein hybrid for bioelectronic applications. Photochem. Photobiol. Sci. 21 (1), 13–22.
Harikesh, P.C., Yang, C.Y., Tu, D., Gerasimov, J.Y., Dar, A.M., Armada-Moreira, A., Massetti, M., Kroon, R., Bliman, D., Olsson, R., Stavrinidou, E., Berggren, M., Fabiano, S., 2022. Organic electrochemical neurons and synapses with ion mediated spiking. Nat. Commun. 13 (1), 901.
Holechek, J.L., Geli, H.M.E., Sawalhah, M.N., Valdez, R., 2022. A global assessment: can renewable energy replace fossil fuels by 2050? Sustainability 14 (8).
Hu, X., Ritz, T., Damjanovic, A., Autenrieth, F., Schulten, K., 2002. Photosynthetic apparatus of purple bacteria. Q. Rev. Biophys. 35 (1), 1–62.
Jaiswal, K.K., Chowdhury, C.R., Yadav, D., Verma, R., Dutta, S., Jaiswal, K.S., SangmeshB, Karuppasamy, K.S.K., 2022. Renewable and sustainable clean energy development and impact on social, economic, and environmental health. Energy Nexus 7.
Kathpalia, R., Verma, A.K., 2021. Bio-inspired nanoparticles for artificial photosynthesis. Mater. Today Proc. 45, 3825–3832.
Keene, S.T., Gkoupidenis, P., Burgt, Y.v.d., 2021. Neuromorphic computing systems based on flexible organic electronics. Organic Flexible Electronics 531–574.
Khoshfetrat, S.M., 2025. In situ synthesis of nickel-substituted zeolitic metal-organic framework on Ti3C2 MXene for enhanced electrocatalytic sensing of L-tryptophan. J. Electroanal. Chem. 992.
Khoshfetrat, S.M., Mamivand, S., Darband, G.B., 2024. Hollow-like three-dimensional structure of methyl orange-delaminated Ti(3)C(2) MXene nanocomposite for high-performance electrochemical sensing of tryptophan. Mikrochim. Acta 191 (9), 546.
Khoshfetrat, S.M., Motahari, M., Mirsian, S., 2025. 3D porous structure of ionic liquid-delaminated Ti(3)C(2) MXene nanosheets for enhanced electrochemical sensing of tryptophan in real samples. Sci. Rep. 15 (1), 6804.
Kornienko, N., Zhang, J.Z., Sakimoto, K.K., Yang, P., Reisner, E., 2018. Semi-artificial photosynthesis: interfacing nature's catalytic machinery with synthetic materials. Nat. Nanotechnol. 13 (10), 890–899.
Labarile, R., Cotugno, P., Ancona, V., Trotta, M., Veronico, P., 2025. Biostimulation effect of Rhodobacter sphaeroides on Arabidopsis thaliana grown in soils contaminated with heavy metals and polychlorinated biphenyls. Current Plant Biology 42.
Lawrence, J.M., Egan, R.M., Hoefer, T., Scarampi, A., Shang, L., Howe, C.J., Zhang, J.Z., 2023. Rewiring photosynthetic electron transport chains for solar energy conversion. Nature Reviews Bioengineering 1 (12), 887–905.
Li, W., Thian, E.S., Wang, M., Wang, Z., Ren, L., 2021. Surface design for antibacterial materials: from fundamentals to advanced strategies. Adv. Sci. (Weinh.) 8 (19), e2100368.
Liu, L.N., Bracun, L., Li, M., 2024. Structural diversity and modularity of photosynthetic RC-LH1 complexes. Trends Microbiol. 32 (1), 38–52.
Lu, Q., Wang, J., Faghihnejad, A., Zeng, H., Liu, Y., 2011. Understanding the molecular interactions of lipopolysaccharides during E. coli initial adhesion with a surface forces apparatus. Soft Matter 7 (19).
Lukashev, E.P., Nadtochenko, V.A., Permenova, E.P., Sarkisov, O.M., Rubin, A.B., 2007. Electron phototransfer between photosynthetic reaction centers of the bacteria Rhodobacter sphaeroides and semiconductor mesoporous tiO2 films. Dokl. Biochem. Biophys. 415, 211–216.
Marquez, A.V., McEvoy, N., Pakdel, A., 2020. Organic electrochemical transistors (OECTs) toward flexible and wearable bioelectronics. Molecules 25 (22).
Mayer, A., 2022. Fossil fuel dependence and energy insecurity. Energy Sustain. Soc. 12 (1).
Mousavi, M.F., Amiri, M., Noori, A., Khoshfetrat, S.M., 2017. A prostate specific antigen immunosensor based on Biotinylated-Antibody/Cyclodextrin inclusion complex: fabrication and electrochemical studies. Electroanalysis 29 (12), 2818–2831.
Musazade, E., Voloshin, R., Brady, N., Mondal, J., Atashova, S., Zharmukhamedov, S.K., Huseynova, I., Ramakrishna, S., Najafpour, M.M., Shen, J.-R., Bruce, B.D., Allakhverdiev, S.I., 2018. Biohybrid solar cells: fundamentals, progress, and challenges. J. Photochem. Photobiol. C Photochem. Rev. 35, 134–156.
Oh, J.K., Yegin, Y., Yang, F., Zhang, M., Li, J., Huang, S., Verkhoturov, S.V., Schweikert, E.A., Perez-Lewis, K., Scholar, E.A., Taylor, T.M., Castillo, A., Cisneros-Zevallos, L., Min, Y., Akbulut, M., 2018. The influence of surface chemistry on the kinetics and thermodynamics of bacterial adhesion. Sci. Rep. 8 (1), 17247.
Operamolla, A., Ragni, R., Milano, F., Tangorra, R.R., Antonucci, A., Agostiano, A., Trotta, M., Farinola, G., 2015. "Garnishing" the photosynthetic bacterial reaction center for bioelectronics. J. Mater. Chem. C 3 (25), 6471–6478.
Peisker, J., 2023. Context matters: the drivers of environmental concern in European regions. Glob. Environ. Change 79.
Pourasl, H.H., Barenji, R.V., Khojastehnezhad, V.M., 2023. Solar energy status in the world: a comprehensive review. Energy Rep. 10, 3474–3493.
Qazi, A., Hussain, F., Rahim, N.A.B.D., Hardaker, G., Alghazzawi, D., Shaban, K., Haruna, K., 2019. Towards sustainable energy: a systematic review of renewable energy sources, technologies, and public opinions. IEEE Access 7, 63837–63851.
Rather, R.A., Wani, A.W., Mumtaz, S., Padder, S.A., Khan, A.H., Almohana, A.I., Almojil, S.F., Alam, S.S., Baba, T.R., 2022. Bioenergy: a foundation to environmental sustainability in a changing global climate scenario. J. King Saud Univ. Sci. 34 (1).
Ravi, S.K., Tan, S.C., 2015. Progress and perspectives in exploiting photosynthetic biomolecules for solar energy harnessing. Energy Environ. Sci. 8 (9), 2551–2573.
Rhodes, C.J., 2010. Solar energy: principles and possibilities. Sci. Prog. 93 (Pt 1), 37–112.
Rivnay, J., Inal, S., Salleo, A., Owens, R.M., Berggren, M., Malliaras, G.G., 2018. Organic electrochemical transistors. Nat. Rev. Mater. 3 (2).
Rondelli, F., Salvo, A.D., Sebastianella, G.C., Murgia, M., Fadiga, L., Biscarini, F., Lauro, M.D., 2023. Pre-synaptic DC bias controls the plasticity and dynamics of three-terminal neuromorphic electrolyte-gated organic transistors. Neuromorph. Comput. Eng. 3 (1).
Ruban, A.V., 2016. Nonphotochemical chlorophyll fluorescence quenching: mechanism and effectiveness in protecting plants from photodamage. Plant Physiol. 170 (4), 1903–1916.
Scheuring, S., Nevo, R., Liu, L.N., Mangenot, S., Charuvi, D., Boudier, T., Prima, V., Hubert, P., Sturgis, J.N., Reich, Z., 2014. The architecture of Rhodobacter sphaeroides chromatophores. Biochim. Biophys. Acta 1837 (8), 1263–1270.
Sekar, N., Umasankar, Y., Ramasamy, R.P., 2014. Photocurrent generation by immobilized Cyanobacteria via direct electron transport in photo-bioelectrochemical cells. Phys. Chem. Chem. Phys. 16 (17), 7862–7871.
Timpmann, K., Chenchiliyan, M., Jalviste, E., Timney, J.A., Hunter, C.N., Freiberg, A., 2014. Efficiency of light harvesting in a photosynthetic bacterium adapted to different levels of light. Biochim. Biophys. Acta 1837 (10), 1835–1846.
Trammell, S.A., Wang, L., Zullo, J.M., Shashidhar, R., Lebedev, N., 2004. Orientated binding of photosynthetic reaction centers on gold using Ni-NTA self-assembled monolayers. Biosens. Bioelectron. 19 (12), 1649–1655.
Utschig, L.M., 2020. Preface to the special issue: photosynthesis-inspired biohybrid and biomimetic systems. Photosynth. Res. 143 (2), 97–98.
van de Burgt, Y., Santoro, F., Tee, B., Alibart, F., 2023. Editorial: focus on organic materials, bio-interfacing and processing in neuromorphic computing and artificial sensory applications. Neuromorph. Comput. Eng. 3 (4).
Walker, J.E., 1998. ATP Synthesis by Rotary Catalysis (Nobel lecture). Angew. Chem. Int. Ed. 37 (17), 2308–2319.
Wang, B., Khoshfetrat, S.M., Mohamadimanesh, H., 2024. Peroxidase-like manganese oxide nanoflowers-delaminated Ti3C2 MXene for ultrasensitive dual-mode and real-time detection of H2O2 released from cancer cells. Microchem. J. 207.
Wang, J., Azam, W., 2024. Natural resource scarcity, fossil fuel energy consumption, and total greenhouse gas emissions in top emitting countries. Geosci. Front. 15 (2).
Yolcan, O.O., 2023. World energy outlook and state of renewable energy: 10-Year evaluation. Innov. Green Dev. 2 (4).
Zhang, L., Xu, M., Chen, H., Li, Y., Chen, S., 2022. Globalization, green economy and environmental challenges: state of the art review for practical implications. Front. Environ. Sci. 10.